*Met. Mater. Int., Vol. 22, No. 6 (2016), pp. 1026~1032*
doi: 10.1007/s12540-016-6386-x

# Phase Formation and Mechanical Properties of Cu-Zr-Ti Bulk Metallic Glass Composites

**Byoung Jin Kim[1], Young Su Yun[1], Won Tae Kim[2], and Do Hyang Kim[1,*]**

[1]Department of Materials Science & Engineering, Yonsei University, Seoul 03722, Republic of Korea
[2]Department of Laser & Optical Information Engineering, Cheongju University, Cheongju 28503, Republic of Korea

(received date: 3 June 2016 / accepted date: 28 June 2016)

The effect of the type of the crystalline phase and its volume fraction on the mechanical property of $Cu_{50}Zr_{50-x}Ti_x$ alloys (x = 0-10) bulk metallic glass composites has been investigated in this study. Up to 6 at% of Ti, B19' phase particles distributed in the glassy matrix, while at 8 and 10% of Ti, B2 phase particles are retained in the glass matrix due to suppression of the eutectoid transformation of B2 phase and by avoidance of martensitic transformation of B2 into B19'. The volume fraction of crystalline phase is strongly dependent on the cooling rate. The larger volume fraction of the crystalline phases results in the lower yield stress, the higher plastic strain, and the more pronounced work hardening behavior. At the crystalline volume fraction below ~30%, the variation of the yield strength can be described by the rule of mixture model (ROM), while at the crystalline volume fraction higher than ~50% by the load-bearing model (LBM). At the crystal fractions between 30 and 50%, there is a yield strength drop and a transition from the ROM to the LBM. This transition is due to the formation of the crystalline structural framework at higher crystal fraction.

**Keywords:** bulk metallic glass composites, mechanical properties, crystal plasticity, compression test, b2 phase

## 1. INTRODUCTION

Bulk metallic glasses (BMGs) with liquid-like disordered atomic structure exhibit some exotic mechanical properties such as high yield strength and large elastic strain limit, wear resistivity together with relatively low Young's modulus [1-3]. However, BMGs show low level of plasticity, since plastic deformation is localized in several tens of nanometer thickness shear bands [4,5]. Therefore, the strain in each shear band is very high, but the total macroscopic plastic strain in the whole sample is very low. That is the reason why BMGs generally fails by a catastrophic fracture without showing any sign of work hardening [6-8]. Such type of deformation behavior of BMGs is evidenced by the serrated flow (work softening) in the stress-strain curve upon compressive loading.

To overcome such a problem in BMGs, there have been great efforts, mainly by introducing various types of heterogeneity in the glassy matrix, for example, ex situ second phase particles [9,10], in situ ductile particles (dendrites) or precipitates [11,12]. The particles or precipitates embedded in the glass matrix play a role in delocalization of shear by branching individual shear bands and preventing their propagation [13]. The multiple shear bands can initiate at the interface between the particles and the glass matrix, leading to enhancement of the plastic strain.

In such BMG matrix composites (BMGCs), the enhancement of the plasticity is strongly affected by the size and volume fraction of the crystalline particles and their distribution in the glassy matrix [14-16]. When ductile particles or dendrites are in micrometer scale, they will deform by dislocation mechanism under loading, providing a plastic strain in BMGCs [17]. Some crystal particles show phase transition during external force condition, showing transformation induced plasticity (TRIP) [18,19]. On the contrary, when nanometer scale precipitates are formed in the glassy matrix, they are not effective in blocking the propagation of shear band, but effective in initiating the multiple shear bands [20].

Among the ductile particle (dendrite) reinforced BMGCs, Cu-Zr based BMGC exhibits significant plastic deformability and pronounced work hardening due to the presence of B2 CuZr particles in the glassy matrix [21]. B2 CuZr tends to undergo martensitic transformation from cubic primitive B2 to monoclinic B19' upon rapid quenching or external loading [22,23]. In order to fabricate Cu-Zr based BMGC with improved mechanical properties, the following three conditions should be met: 1) retention of the glass forming ability of the glassy matrix; 2) preservation of B2 CuZr phase in as-cast glassy

---

*Corresponding author: dohkim@yonsei.ac.kr matrix; and 3) occurrence of martensitic transformation during loading (deformation-induced martensitic transformation). It has been shown that minor element additions such as Al, Ti, Ag and rare earth metals can improve the glass forming ability of Cu-Zr alloys [24-26]. To preserve the B2 phase in the as-cast state, it is important to avoid the martensitic transformation of B2 during solidification. In shape memory alloys like Cu-Zr and Ti-Ni systems, B2 phase mostly transforms into martensite during manufacturing process [22,27,28]. Recently, it has been shown that the addition of Ti in Cu-Zr alloy lowers the martensite start temperature ($M_s$), for example, with Ti content increasing from 0 at% to 10 at%, the value of $M_s$ decreases from ~435 K to ~246 K, indicating that B2 CuZr can be preserved after solidification [29]. On the other hand, it has been reported that the addition of Ti destabilizes the B2 formation by increasing the eutectoid temperature ($B2 \rightarrow Cu_{10}Zr_7 + CuZr_2$ at 988 K in binary Cu-Zr system) and by decreasing the liquidus temperature [21].

Although there are reports on the effect of Ti addition on the microstructural evolution of Cu-Zr BMGCs, their mechanical properties has not been investigated in detail. Therefore, the aim of the present study is to investigate the effect of Ti addition on the microstructure evolution and mechanical properties in Cu-Zr based BMGCs. Special emphases were placed on the preservation of the B2 CuZr in as-cast state, deformation-induced martensitic transformation, and effect of its volume fraction on the plasticity.

## 2. EXPERIMENTAL PROCEDURE

The alloy ingots with nominal compositions of $Cu_{50}Zr_{50-x}Ti_x$ (x=0, 2, 4, 6, 8 and10 at%) were prepared by arc melting of high purity elemental constituents (99.95% or higher) under a Ti-gettered argon atmosphere. For homogeneous distribution of the elements the melting procedure was repeated over five times. The ingots were prepared by suction casting into copper mold having cylindrical cavity with a length of 50 mm and various diameters of 1, 2, 3 and 4 mm. The structure of suction-cast samples was verified using x-ray diffraction (XRD, Rigaku, CN2301, Tokyo, Japan) with monochromatic CuKα radiation source (λ = 1.5405 Å). Microstructural analysis of as-cast and deformed samples was performed by scanning electron microscopy (JEOL$^{TM}$, JSM 7001F) and transmission electron microscopy (TEM, GEOL$^{TM}$, JEM2100F, Tokyo, Japan) coupled with energy-dispersive x-ray analysis (EDS, Oxford Instruments INCA, UK). TEM specimens were prepared by an ion milling method (Precision Ion Polishing System, Gatan Model 691, Vienna, OH) after mechanical thinning. Mechanical property was evaluated by compression test (UTM, ZWICK, Z050 TN). The samples with an aspect ratio of 2:1 were tested at room temperature under a quasi-static loading condition with an initial strain rate of $10^{-4}$/s. At least three samples were tested to evaluate the compression properties of the cast-rod.

## 3. RESULTS

Table 1 summarized the microstructural characteristics of as-cast x = 0-10 alloys depending on the sample diameter. In 1 mm diameter sample, all the alloys investigated consisted of a monolithic glass phase. When the diameter is over 2 mm, the crystalline phase began to appear, forming BMGCs. The noticeable microstructural features are: 1) In x = 0-6 alloys, the volume fraction of B19' tends to increase with increasing the sample diameter, reaching ~100% in 4 mm diameter sample; 2) In x = 8-10 alloys, the volume fraction of B2 tends to increase with increasing the sample diameter, reaching ~65% in 4 mm diameter sample; 3) Even in same diameter sample, the volume fraction of the crystalline phase is different due to difference in local cooling rate. In particular, B2 phase is retained in the glass matrix, when the amount of Ti exceeds 8 at% in $Cu_{50}Zr_{50-x}Ti_x$ alloys.

Figure 1(a) and (b) show XRD patterns obtained from the upper region of the as-cast x = 0 and x = 8 alloys with the diameters of 1, 2, 3 and 4 mm, confirming the results in Table 1. The XRD patterns from 1 mm diameter samples from x = 0 and 8 alloys exhibited a diffuse halo peak, indicating presence of

**Table 1.** Microstructural features of as-cast x = 0 - 10 alloys depending on the sample diameter (1. Results on upper region and lower region were obtained from the section 2 cm and 4 cm, respectively, from the bottom in 5cm long sample; 2. The volume fraction of the crystalline phase is an average value obtained from at least 3 samples.)

| | 1 mm | | 2 mm | | | | 3 mm | | | | 4 mm | |
|---|---|---|---|---|---|---|---|---|---|---|---|---|
| | | | Lower region | | Upper region | | Lower region | | Upper region | | Lower region | |
| | Phase type | Crystal volume fraction (%) | Phase type | Crystal volume fraction (%) | Phase type | Crystal volume fraction (%) | Phase type | Crystal volume fraction (%) | Phase type | Crystal volume fraction (%) | Phase type | Crystal volume fraction (%) |
| $Cu_{50}Zr_{50}$ | Glass | 0 | B19' | 5 ± 3 | B19' | 13 ± 2 | B19' | 26 ± 2 | B19' | 64 ± 6 | B19’ | ~100 |
| $Cu_{50}Zr_{48}Ti_2$ | Glass | 0 | B19' | 3 ± 3 | B19' | 14 ± 1 | B19' | 24 ± 1 | B19' | 65 ± 10 | B19’ | ~100 |
| $Cu_{50}Zr_{46}Ti_4$ | Glass | 0 | B19' | 2 ± 3 | B19' | 14 ± 1 | B19' | 25 ± 1 | B19' | 64 ± 10 | B19’ | ~100 |
| $Cu_{50}Zr_{44}Ti_6$ | Glass | 0 | B19' | 1 ± 2 | B19' | 13 ± 1 | B19' | 22 ± 1 | B19' | 64 ± 13 | B19’ | ~100 |
| $Cu_{50}Zr_{42}Ti_8$ | Glass | 0 | Glass | 0 | B2 | 1 ± 3 | B2 | 6 ± 3 | B2 | 19 ± 1 | B2 | 64 ± 8 |
| $Cu_{50}Zr_{40}Ti_{10}$ | Glass | 0 | Glass | 0 | B2 | 1 ± 4 | B2 | 8 ± 2 | B2 | 20 ± 2 | B2 | 68 ± 6 |

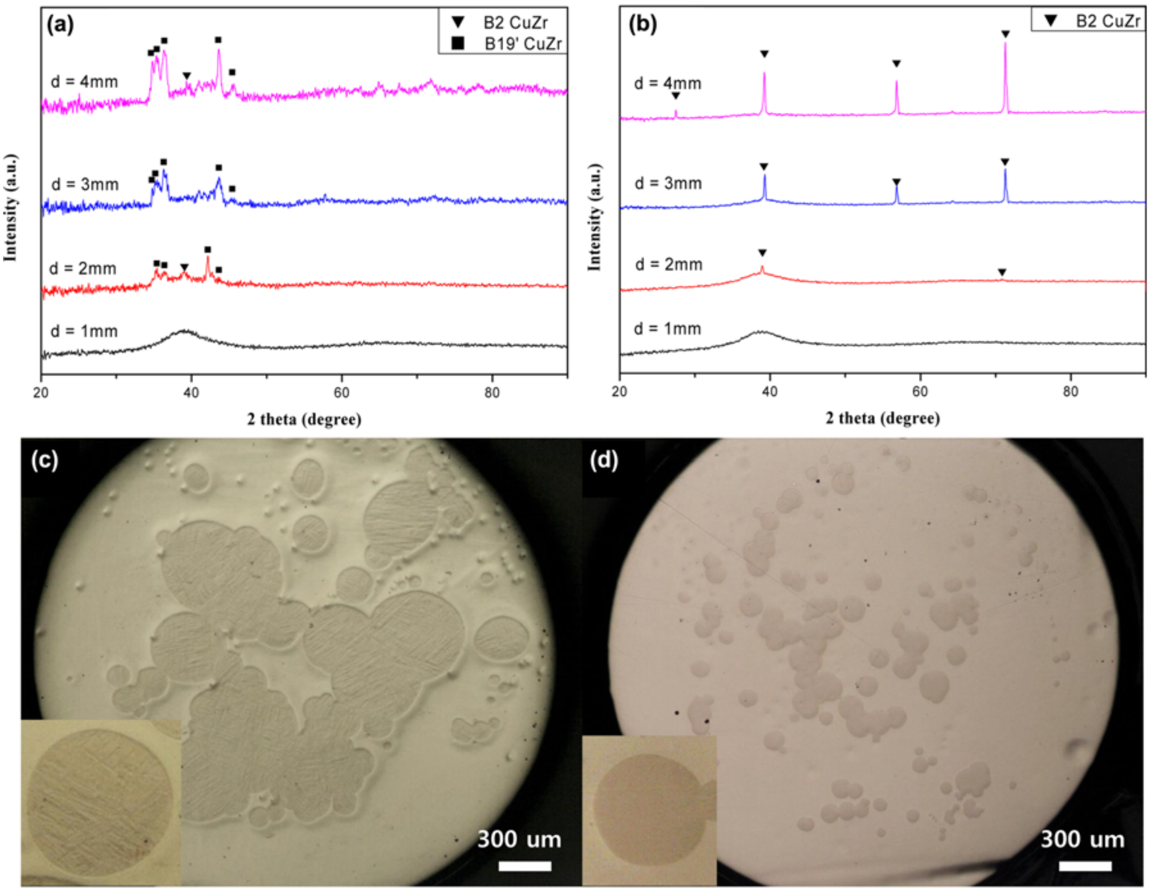

**Fig. 1.** XRD patterns obtained from: (a) as-cast x = 0 alloy; and (b) as-cast x = 8 alloy. OM images obtained from: (c) as-cast x = 0 alloy (crystal fraction: 58%); and (d) as-cast x = 8 alloy (crystal fraction: 18%). The insets are BSE images showing the internal structure of the particles.

a single glass phase. The XRD patterns from 2-4 mm samples exhibited sharp diffraction peaks from B19' in x = 0 alloy and B2 in x = 8 alloy. In both alloys, the intensity from the crystalline phases increased with increasing sample diameter, indicating an increase of crystal volume fraction with slower cooling rate. The XRD patterns from x = 0 alloy (diameter: 2-4 mm) indicate that very tiny amount of B2 is present in the glassy matrix, although B19' is the major crystalline phase. Figures 1(c) and (d) show optical microscope (OM) images obtained from the upper region of the as-cast x = 0 and x = 8 alloys with the diameter of 3 mm. The individual second phase particles were almost spherical, and the diameters were ~ 200 μm and ~60 μm in x = 0 and 8 alloys, respectively. Frequently, the particles agglomerated together, forming large size particles, i.e. ~800 μm in x = 0 alloy and ~200 μm in x = 8 alloy. In both alloys, most of the individual and agglomerated particles were present in the center region of the rods, and their distribution was not uniform. Although the general microstructural features were similar in both alloys, the size scale of the particles in x = 8 alloy is smaller than in x = 0 alloy due to narrower stability region of B2 and higher glass forming ability with the addition of Ti [21,25]. The present result also indicates that the cooling rate is high enough to bypass the decomposition of B2 phase into other equilibrium crystalline phases. The back scattered electron (BSE) image inserted in Fig. 1(c) shows a microstructural feature typical of martensitic lath from B19' phase, while that inserted in Fig. 1(d) shows no noticeable microstructural features from B2 phase.

Figure 2(a) shows uniaxial compression engineering stress-strain curves obtained from 1 mm, 2 mm (lower region), and 3 mm (upper and lower region) samples of x = 0 alloy, while Fig. 2(b) from 1 mm, 2 mm (upper region), 3 mm (upper region) and 4 mm samples of x = 8 alloy. Since the fraction of B19' in lower region of 2 mm, and lower and upper region of 3 mm samples in x = 0 alloy were ~5, ~25 and ~75%, respectively, it can be noticed that 2% offset yield strength decreased significantly with increasing B19' fraction, i.e. from ~1830 MPa in monolithic glass alloy down to ~780 MPa in the alloy with B19' fraction of ~75%. On the other hand, the fracture strain increased from ~1.9% in monolithic glass alloy up to ~10.1% in the alloy with B19' fraction of ~75%. The fraction of B2 in upper region of 2, 3 and 4 mm samples in x = 8 alloy were ~5, ~20 and ~70%, respectively, and 2% offset yield strength decreased from ~1850 MPa in monolithic glass alloy down

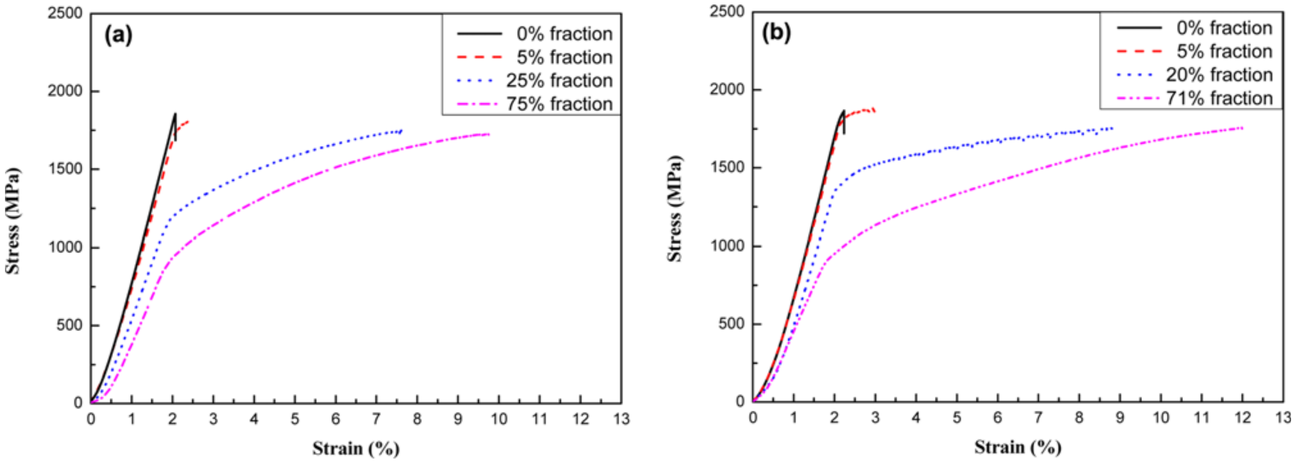

**Fig. 2.** Engineering stress-strain curves obtained from: (a) as-cast x = 0 alloy with the diameters of 1 mm, 2 mm (lower region), 3 mm (lower and upper region); and (b) as-cast x = 8 alloy with the diameters of 1, 2 (upper region), 3 (upper region) and 4 mm (lower region).

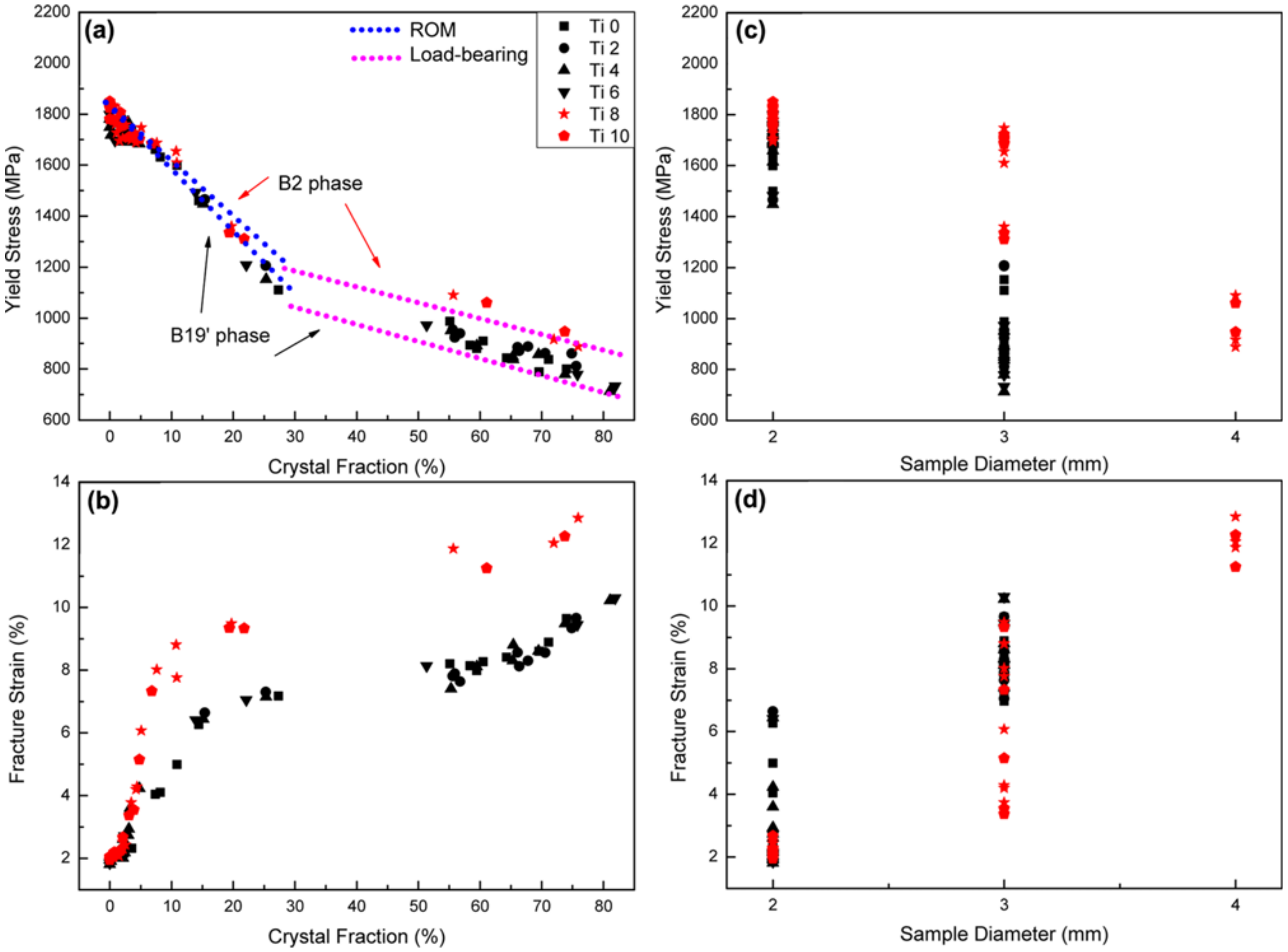

**Fig. 3.** Mechanical properties of Cu$_{50}$Zr$_{50-x}$Ti$_x$ alloys (x = 0, 2, 4, 6, 8, 10): (a) 2% offset yield strength; and (b) fracture strain as a function of crystal fraction; and (c) 2% offset yield strength; and (d) fracture strain as a function of sample diameter. Data marked by black symbols are B19' phase and red symbols are B2 phase.

to ~830 MPa in the alloy with B2 fraction of ~70%. The fracture strain increased from ~2% in monolithic glass alloy up to ~12.2% in the alloy with B2 fraction of ~70%. Here, the interesting results to be pointed out are: 1) the fracture strain in both alloys increases rapidly, when the effective volume fraction exceeds 5%; 2) x = 8 alloy shows higher plasticity than x = 0 alloy under the condition of similar crystal fraction; and 3) work hardening behavior is more pronounced with the increase of crystal volume fraction.

To investigate more systematically the effect of Ti addition on the mechanical properties of Cu-Zr alloy, the data obtained in the present study are displayed in Fig. 3. Figures 3(a) and (b) show the variation of yield stress and fracture strain for x = 0-10 alloys as a function of volume fraction of the crystalline phase in 2, 3 and 4 mm diameter rod samples. As already pointed out in Fig. 2, the fracture strain increased, and the yield stress decreased with the increase of the crystal volume fraction, irrespective of the type of the crystalline phase. As can be seen in Fig. 3(a), the yield strength of B19' and B2 reinforced BMGCs decreased with an almost same rate with increasing crystal fraction except slightly higher yield strength of B2 sample when the crystal fraction is higher than ~10%. Figure 3(b) shows that the fracture strain of both B19' and B2 samples increased sharply when the crystal fraction is larger than ~5%, but B2 sample exhibited higher level of fracture strain, for example, 9% and 6.5% for B2 reinforced BMGC and B19' reinforced BMGC, respectively, at ~20% volume fraction. The fracture strain reaches up to 13 and 10% for B2 and B19' BMGCs, respectively, at ~80% volume fraction. Figures 3(c) and (d) show the variation of yield stress and fracture strain as a function of rod diameter (2, 3 and 4 mm). Rather scattered values of yield strength and fracture strain were observed, particularly for 3 mm rod, due to the effect of the difference in local cooling rate, as explained above. The result indicates that the mechanical properties in Cu-Zr based BMGC are better evaluated as a function of crystal volume fraction rather than cast rod diameter.

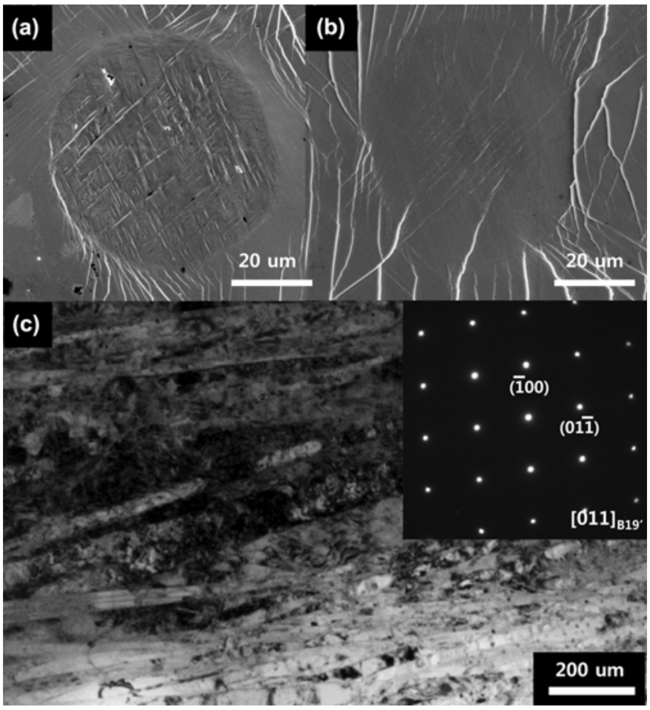

**Fig. 4.** SE images showing particle and surrounding matrix after compression test obtained from: (a) x = 0 alloy (lower region of 3 mm diameter sample); (b) x = 8 alloy (upper region 3 mm diameter sample); and (c) BF image showing the microstructure inside the particle after compression test (upper region of 3 mm diameter sample). The inset is the corresponding SADP.

Figures 4(a) and (b) show secondary electron (SE) images of the particle and the surrounding matrix after compression of x = 0 and 8 alloys, respectively. In the case of x = 0 alloy, martensitic lath structure which formed during solidification is clearly visible inside the B19' phase particle. In the surrounding matrix, the shear bands are bent in the vicinity of the B19' phase particle and eventually their propagation is blocked, forming narrow shear steps at the boundary. In case of x = 8 alloy martensitic lath structure is observed, although it is not clearly visible as in Fig. 4(a). It is evident that the lath structure formed by deformation during compression test. In the surrounding matrix, many shear bands with larger shear steps than those in x = 0 alloy formed during deformation. In particular, some of the shear bands intruded inside particle, bringing about the deformation induced martensitic transformation inside the B2 phase particle. Figure 4(c) shows bright field (BF) TEM image clearly revealing the martensitic lath structure inside the particle after deformation of x = 8 alloy. The selected area diffraction pattern (SADP) was identified as [011] zone of B19' structure.

## 4. DISCUSSION

In $Cu_{50}Zr_{50}$ alloy B2 structure of the primary phase particles formed in the liquid state transforms into B19' martensitic structure by thermal stress occurred during cooling in the solid state, as reported previously [21]. When up to 6 at% of Zr is replaced with Ti in $Cu_{50}Zr_{50}$ alloy, martensitic transformation of B2 phase particles still occurs during cooling, forming B19' phase particles distributed in the glassy matrix. However, when 8-10 at% of Zr is replaced with Ti, no martensitic transformation occurs during cooling, therefore, B2 phase particles are retained in the glass matrix after solidification. From the previous reports, the effects of addition of Ti in Cu-Zr alloy can be summarized: 1) enhancement of glass forming ability [25]; 2) suppression of martensitic transformation of B2 into B19' by lowering the $M_s$ temperature [29]; and 3) destabilization of B2 formation during solidification by increasing the eutectoid temperature (B2 $\rightarrow$ $Cu_{10}Zr_7$ + $CuZr_2$) and as well as by decreasing the liquidus temperature [21]. In the present study, the eutectoid transformation of B2 phase is suppressed by properly high cooling rate, and the martensitic transformation into B19' is avoided due to lowered $M_s$ temperature. Therefore, B2 structure can be retained after solidification in solid state, resulting in the B2 phase reinforced BMGC in $Cu_{50}Zr_{50-x}Ti_x$ alloys (x = 8 and 10).

The volume fraction of crystalline phase is strongly dependent on the cooling rate, i.e. on the sample diameter, and even on the position in a single cast-rod (Table 1). Therefore, the fraction of B19' increases with lower cooling rate in $Cu_{50}Zr_{50-x}Ti_x$ alloys (x = 0-6, B19' BMGC), while that of B2 increases in $Cu_{50}Zr_{50-x}Ti_x$ alloys (x = 8 and 10, B2 BMGC). The yield strength and fracture stain of the BMGCs generally exhibit a good correlation with the crystalline volume fraction (Fig. 3). The larger volume fraction of the crystalline phases results in the lower yield stress, the higher plastic strain, and the more pronounced work hardening behavior. However, there are some differences depending on the type of the crystalline phase: 1) The yield strength of B2 BMGC is slightly higher than that of B19' BMGC when the crystalline fraction is over ~10%; and 2) The fracture strain of both B2 and B19' BMGCs sharply increases when the crystal fraction is over ~5%, over which B2 BMGC shows ~2% higher fracture strain than B19' BMGC up to ~80% of the crystal fraction.

When the crystalline volume fraction is lower than ~30%, the variation of the yield strength, $\sigma_{composite}$ can be described by the rule of mixtures (ROM) as shown below:

$$\sigma_{composite} = f_{amorphous}\sigma_{amorphous} + f_{crystalline}\sigma_{crystalline} \quad (1)$$

, where f and σ represent the volume fraction and the yield stress of the amorphous phase or crystalline phase. In this regime, the glass matrix has a significantly higher strength than B2 or B19' crystalline phases, therefore, yielding of the BMGC is controlled by yielding of the relatively harder glass matrix, as marked in Fig. 3(a). For the calculation, $\sigma_{amorphous}$, $\sigma_{crystalline\ B2'}$ and $\sigma_{crystalline\ B19'}$ are considered to be 1850 MPa, 750 MPa and 600 MPa, respectively [30].

On the other hand, when the crystal fraction is higher than ~50%, the composite can be considered as the crystalline phase matrix composite reinforced by the glass phase. Therefore, in this regime, the strengthening behavior can be modelled by the load-bearing model (LBM) shown below:

$$\sigma_{composite} = \sigma_{crystalline}\,(1 + 0.5f_{amorphous}) \quad (2)$$

Pauly *et al.* [31] and Gargarella *et al.* [32] have shown that the variation of yield strength below ~30% of B2 fraction is controlled by the ROM model, while that above ~50% by the LBM in Cu-Zr-Al and Ti-Cu-Ni-Zr B2 reinforced BMGCs, of which the result is similar to the present study. However, Castellero *et al.* [30] have reported that only ROM model can be adopted for the whole crystal fraction range up to ~90% in Cu-Zr-Al B2 reinforced BMGC. As shown in Fig. 3(a), at the crystal fractions between ~30 and ~50%, there is an obvious drop in the yield strength and a transition from the ROM to the LBM. This transition has been interpreted to be ascribed to a change in the microstructure. At low crystal fraction below ~30%, the near-spherical particles are separated and some particles begin the impinge each other, while at high crystal fraction above ~50%, most crystalline particles agglomerate each other, forming a crystalline structural framework as shown in Fig. 1(c). This microstructural change can be linked to yield strength drop as well as fracture strain increase shown in Figs. 3(a) and (b).

It has been reported that, ~30% critical value of crystal fraction is the maximum value to increase the fracture strain up to ~23 and ~13% in Ti-Cu-Ni-Zr BMGC and Cu-Zr-Al BMGC, respectively [31,32]. In refs [31,32], the fracture strain decreases with further increasing the crystal fraction over ~30%. In the present study, the values of the fracture strain at ~30% crystal fraction in B2 and B19' BMGCs are ~10% and ~7%, respectively. However, the fracture continues to increase when the crystal fraction reached ~80%.

The present study shows that B19' BMGC exhibits a moderate combination of strength and ductility, although it is inferior to B2 BMGC. It has been shown that CoZr B33 martensite BMGC exhibit a relatively high fracture strain of 5~15% in Co-Zr-Ni and Co-Zr-Pd BMGC, although the value is lower than ~20% of B2 BMGC [33,34].

B2 phase has high-order symmetry of cubic but amorphous has no long-range ordering. Such a periodicity mismatch at the interface generates shear bands during compressive loading. It has been shown that the elastic properties of the glassy phase and the B2 crystals are nearly identical. Therefore, no local stress concentration arises at the glass–crystal interface during compressive loading. But martensitic transformation during loading generates shear band as shown in Fig. 4.

## 5. CONCLUSIONS

The effects of crystal phase and crystal fraction on the mechanical property in $Cu_{50}Zr_{50-x}Ti_x$ alloys (x = 0-10) have been investigated in the present study. The conclusions are as follows:

(1) When up to 6 at% of Zr is replaced with Ti in $Cu_{50}Zr_{50}$ alloy, martensitic transformation of B2 phase particles occurs during cooling, forming B19' phase particles distributed in the glassy matrix. However, when 8-10 at% of Zr is replaced with Ti, no martensitic transformation occurs, therefore, B2 phase particles are retained in the glass matrix after solidification. Such a microstructural evolution can be explained by suppression of the eutectoid transformation of B2 phase by properly high cooling rate, and by avoidance of the martensitic transformation due to low $M_s$ temperature.

(2) The volume fraction of crystalline phase is strongly dependent on the cooling rate. As a result, the fraction of B19' increases with lower cooling rate in $Cu_{50}Zr_{50-x}Ti_x$ alloys (x = 0-6), while that of B2 increases in $Cu_{50}Zr_{50-x}Ti_x$ alloys (x = 8 and 10). The larger volume fraction of the crystalline phases results in the lower yield stress, the higher plastic strain, and the more pronounced work hardening behavior. The yield strength of B2 BMGC is slightly higher than that of B19' BMGC when the crystalline fraction is over ~10%. The fracture strain of both B2 and B19' BMGCs sharply increases when the crystal fraction

is over ~5%, over which B12 BMGC shows ~2% higher fracture strain than B19’ BMGC up to ~80% of the crystal fraction.

(3) At the crystalline volume fraction below ~30%, the variation of the yield strength can be described by the ROM model, while at the crystalline volume fraction higher than ~50% by the LBM. At the crystal fractions between 30 and 50%, there is an obvious drop in the yield strength and a transition from the ROM model to the LBM. This transition is due to the formation of the crystalline structural framework at higher crystal fraction. The values of the fracture strain at ~30% crystal fraction in B2 and B19’ BMGCs are ~10% and ~7%, respectively. The fracture strain continues to increase when the crystal fraction reached ~80%.

## ACKNOWLEDGMENTS

This work was supported by the National Research Foundation of Korea (NRF) grant funded by the Korea government (MEST) (2016R1A2B2013838). B.J. Kim acknowledges the support from the six times Stage of Brain Korea 21 Project in 2011.

## REFERENCES

1. A. L. Greer, *Science* **267**, 1947 (1995).
2. M. F. Ashby and A. L. Greer, *Scripta Mater.* **54**, 321 (2006).
3. B.-T. Jang, Y.-I. Kim, and S.-H. Yi, *Korean J. Met. Mater.* **53**, 519 (2015).
4. A. Inoue and A. Takeuchi, *Acta Mater.* **59**, 2243 (2011).
5. X. H. Du, J. C. Huang, H. M. Chen, H. S. Chou, Y. H. Lai, P. K. Liaw, *et al.*, *Intermetallics* **17**, 607 (2009).
6. C. P. P. Chou and F. Spaepen, *Acta Metall.* **23**, 609 (1975).
7. G. He, W. Löser, J. Eckert, and L. Schultz, *Mat. Sci. Eng. A* **352**, 179 (2003).
8. R. Li, S. Pang, H. Men, C. Ma, and T. Zhang, *Scripta Mater.* **54**, 1123 (2006).
9. H. Choi-Yim and W. L. Johnson, *Appl. Phys. Lett.* **71**, 3808 (1997).
10. R. D. Conner, R. B. Dandliker, and W. L. Johnson, *Acta Mater.* **46**, 6089 (1998).
11. Y. S. Oh, C. P. Kim, S. Lee, and N. J. Kim, *Acta Mater.* **59**, 7277 (2011).
12. E. S. Park and D. H. Kim, *Acta Mater.* **54**, 2597 (2006).
13. M. Chen, *Annu. Rev. Mater. Res.* **38**, 445 (2008).
14. M. L. Lee, Y. Li and C. A. Schuh, *Acta Mater.* **52**, 4121 (2004).
15. S. H. Hong, J. T. Kim, M. W. Lee, J. M. Park, M. H. Lee, K. B. Kim, *et al.*, *Metall. Mater. Trans. A* **45**, 2376 (2014).
16. S. H. Hong, J. T. Kim, H. J. Park, Y. S. Kim, J. M. Park, K. B. Kim, *et al.*, *Appl. Microsc.* **45**, 37 (2015).
17. D. C. Hofmann, J. Y. Suh, A. Wiest, G. Duan, M. L. Lind, M. D. Demetriou, and W. L. Johnson, *Nature* **451**, 1085 (2008).
18. S. H. Hong, J. T. Kim, H. J. Park, J. Y. Suh, K. R. Lim, Y. S. Na, J. M. Park, and K. B. Kim, *Intermetallics* **62**, 36 (2015).
19. E. S. Park and D. H. Kim, *Met. Mater. Int.* **11**, 19 (2005).
20. Y. H. Liu, G. Wang, R. J. Wang, D. Q. Zhao, M. X. Pan, and W. H. Wang, *Science* **315**, 1385 (2007).
21. S. Pauly, J. Das, J. Bednarcik, N. Mattern, K. B. Kim, D. H. Kim, and J. Eckert, *Scripta Mater.* **60**, 431 (2009).
22. K. K. Song, S. Pauly, Y. Zhang, P. Gargarella, R. Li, J. Eckert, *et al.*, *Acta Mater.* **59**, 6620 (2011).
23. Y. Wu, Y. Xiao, G. Chen, C. T. Liu, and Z. Lu, *Adv. Mater.* **22**, 2770 (2010).
24. P. Yu, H. Y. Bai, and W. H. Wang, *J. Mater. Res.* **21**, 1674 (2006).
25. H. Men, S. J. Pang, and T. Zhang, *Mat. Sci. Eng. A* **408**, 326 (2005).
26. W. Zhang and A. Inoue, *J. Mater. Res.* **21**, 234 (2006).
27. H.-J. Jun, K. S. Lee, C. P. Kim, and Y. W. Chang, *Met. Mater. Int.* **14**, 297 (2008).
28. T.-H. Nam, J.-Y. Jang, and E.-S. Kim, *Korean J. Met. Mater.* **53**, 451 (2015).
29. Y. N. Koval, G. S. Firstov, L. Delaey, and J. V. Humbeeck, *Scripta Metall. Mater.* **31**, 799 (1994).
30. A. Castellero, T. A. Baser, J. Das, P. Matteis, J. Eckert, L. Battezzati, and M. Baricco, *J. Alloy. Compd.* **509**, S99 (2011).
31. S. Pauly, G. Liu, G. Wang, U. Kühn, N. Mattern, and J. Eckert, *Acta Mater.* **57**, 5445 (2009).
32. P. Gargarella, S. Pauly, M. Samadi Khoshkhoo, U. Kühn, and J. Eckert, *Acta Mater.* **65**, 259 (2014).
33. M. Matsuda, K. Hayashi, and M. Nishida, *Mater. Trans.* **50**, 2335 (2009).
34. M. Matsuda, T. Nishimoto, Y. Morizono, S. Tsurekawa, and M. Nishida, *Intermetallics* **19**, 894 (2011).